Engineering Geology 237 (2018) 64–75

Contents lists available at ScienceDirect

Engineering Geology

journal homepage: www.elsevier.com/locate/enggeo

Dynamic numerical investigation of a stepped-planar rockslide in the Central Andes, Chile

Manuel García[a], César Pastén[b,*], Sergio A. Sepúlveda[c,e], Gonzalo A. Montalva[d]

[a] Department of Geology, University of Chile, Chile
[b] Department of Civil Engineering, University of Chile, Av. Blanco Encalada 2002, Of. 431, Santiago 8370449, Chile
[c] Department of Geology, University of Chile, Chile
[d] Department of Civil Engineering, University of Concepción, Chile
[e] Institute of Engineering Sciences, University of O'Higgins, Chile

ARTICLE INFO

Keywords:
Rockslide
Earthquake
UDEC
Topographic amplification
Dynamic modelling
Earthquake-induced displacements

ABSTRACT

In this paper, static and dynamic analyses were performed considering the reconstituted geometry of a pre-historic 0.1 km^2 rockslide with an exposed stepped-planar failure surface using a distinct element code (UDEC®). The rockslide occurred on the northern slope of the Cerro Catedral mount, located in the headers of the Maipo river drainage basin (Main range of the Andes Cordillera) at the latitude of the Santiago city, Chile, between the Late Pleistocene and the Holocene. The remaining failure surface consists of two distinct sliding planes dipping at an angle of ~37° and connected by a sub-vertical step. The original geometry of the rock slope was estimated from a terrestrial laser scan elevation model (LIDAR), the deposit that remained in the valley, and the hill surface topography. The laser scan of the sliding surfaces and Schmidt hammer field measurements allowed the estimation of the sliding surface mechanical properties, whereas laboratory test results were used to estimate the rock mass material properties. Results from 2D static numerical analyses indicate that the rock slope requires the presence of at least one rock bridge at the sliding surface connecting step in order to be statically stable. Furthermore, we studied the effect of different acceleration time histories recorded during shallow crustal earthquakes, compatible with the regional seismicity, in the rockslide response. The dynamic numerical analyses show that the input earthquake records induce a pronounce topographic amplification in the rock slope, that the rockslide displacement highly correlates with the Arias Intensity, the peak velocity, and the peak acceleration calculated in the rock slope center of gravity, and that the rockslide may have been triggered by horizontal accelerations larger than 0.6 g in the free field. Finally, the slope's response is evaluated under the coupled action of horizontal and vertical accelerations.

1. Introduction

Subduction of the Nazca plate underneath the South American plate causes numerous earthquakes due to the stress accumulation and relief along the Chilean territory (Udias et al., 2012). As a consequence, many natural slopes near the Chilean coastline and in the central valleys of the Andean mountains have been affected by amplification of seismic waves and slope displacements (Antinao and Gosse, 2009; Sepulveda et al., 2008, Sepúlveda et al., 2010; Welkner et al., 2010). In the Maipo river valley (Fig. 1), a translational rockslide occurred in the Cerro Catedral mount that belongs to a larger group of massive slides of Late Pleistocene and Holocene age (Antinao and Gosse, 2009), known as La Engorda landslide complex (Sepúlveda et al., 2012). The rockslide material formed a vast deposit of approximately 0.63 km^2 across the valley, partially covering the riverbed and the nearby hill slopes. The sliding-slope shows a highly regular surface of nearly 400 m width that forms a bedding plane-step sequence before reaching the main scarp towards the top of the mount (Sepúlveda et al., 2012). Fig. 1 shows the south-side view of the sliding surface, along with the aerial view of the zone and the estimated area covered by the deposit. The original hill geometry and the failure mechanism arise as questions.

One of the triggering mechanisms of the rockslide can be attributed to the crustal seismic activity of the region according to Sepúlveda et al. (2012). Triggering of landslides and rockslides depend on the energy, the frequency content, the directivity, and the peak ground acceleration during an earthquake as well as on topographic singularities (Lenti and Martino, 2012, and examples therein). However, attenuation of large mega-thrust earthquakes restricts the ground motion shaking at

* Corresponding author.
E-mail addresses: mangarci@ing.uchile.cl (M. García), cpasten@ing.uchile.cl (C. Pastén), sesepulv@ing.uchile.cl (S.A. Sepúlveda), gmontalva@udec.cl (G.A. Montalva).

https://doi.org/10.1016/j.enggeo.2018.02.001
Received 16 September 2017; Received in revised form 13 January 2018; Accepted 4 February 2018
Available online 10 February 2018
0013-7952/

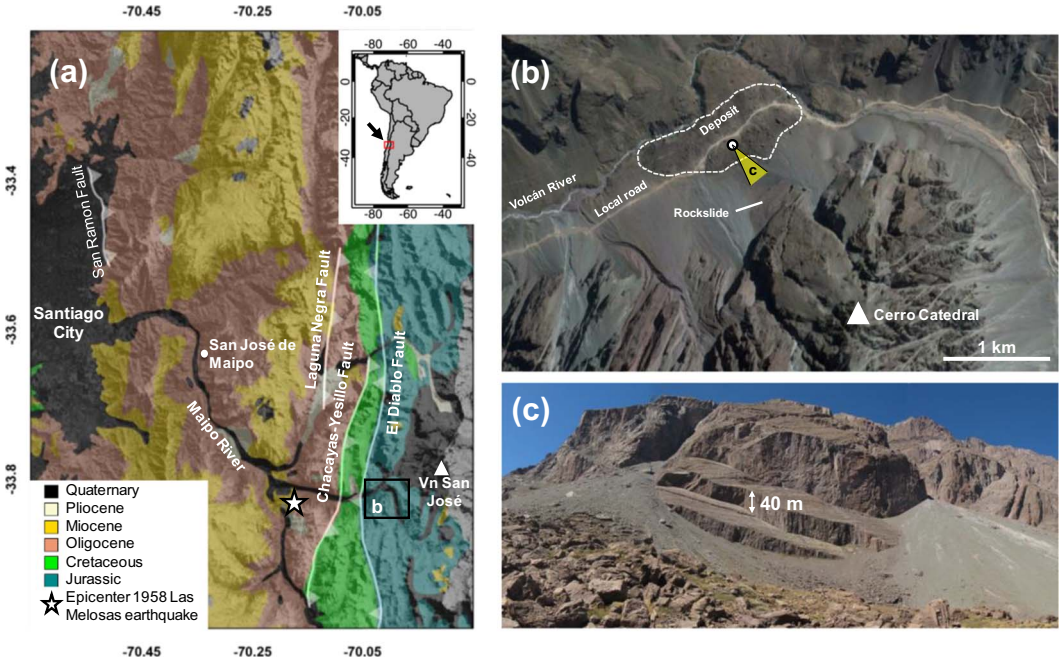

Fig. 1. Study area. (a) Santiago city and the Maipo river valley, (b) aerial view of the rock slope and the deposit, and (c) south-side view of the rock slope.

distances where the rock slope is located. For example, a hypothetical mega earthquake of magnitude Mw = 8.8, similar to the 2010 Maule earthquake (Moreno et al., 2012), with a rupture area A = 61,000 km^2, located in front of the Metropolitan Region, would cause a peak ground acceleration PGA ranging from 0.08 to 0.16 g at a distance of 150 km, depending on the attenuation relationship adopted (Contreras and Boroschek, 2012; Idini et al., 2017; Montalva et al., 2017).

Deterministic and probabilistic limit-equilibrium back analyses of the slope stability, considering a simple slope geometry that consists of four planar failure planes and a slope angle of 44°, indicate that the rock slope would be statically stable and may fail under pseudo-static conditions when horizontal and vertical seismic coefficients of 0.35 are applied (Sepúlveda et al., 2012). In this case, the joints were characterized with a Barton-Bandis failure criterion, adopting joint roughness coefficients (JRC) larger than the values considered in this study. The relatively high seismic coefficients, associated to large peak accelerations, are compatible with the crustal seismic activity of the region (Barrientos et al., 2004; Pérez et al., 2014). For instance, peak horizontal accelerations as high as 1 g were estimated from landslides back-analyses using the Newmark's method during the nearby Las Melosas Mw 6.3 earthquake in 1958 (epicenter in Fig. 1a) (Sepulveda et al., 2008). In addition, these shallow crustal earthquakes have proven to be more destructive than thrust earthquakes because of their radiation patterns and reduced focal distance.

Numerical methods can be used to evaluate the stability of jointed rock slopes (Lin et al., 2012; Mavrouli et al., 2009) and to back-analyze failed slopes (Sturzenegger and Stead, 2012). These methods, unlike traditional analytical methods for rockslide analysis, can easily incorporate the plastic behavior of the involved rock masses and joints (Bhasin and Kaynia, 2004; Chen and Zhao, 1998; Choi and Chung, 2004; Chuhan et al., 1997; Gischig et al., 2015; Kveldsvik et al., 2009; Liu et al., 2014; Souley and Homand, 1996; Zhao et al., 2008), complex failure modes (Stead et al., 2006), and wave propagation through fractured rock (Zhao et al., 2008) that can aggravate the slope stability. In this paper, we use the 2D distinct element method software UDEC (Itasca, 2016) to analyze the possibility that the translational rockslide in the Cerro Catedral mount may have been seismically triggered. Static and dynamic analyses were performed considering a reconstituted geometry of the rock slope. The methodology developed in this paper can help in estimating the geologic and seismic hazard in areas dominated by active faulting and lack of instrumental data.

2. Geological and seismological framework

The study area (33.8°S, 70.0°W; Fig. 1), located in the Main Range of the Andes, is composed by Tertiary volcanic, volcano-sedimentary rocks (the Abanico and the Farellones Formations) and intrusive rocks in its westernmost part, as well as marine and continental Mesozoic sedimentary and volcanic rocks in its eastern part (Fock, 2005; Thiele, 1980). The area is located at the confluence of several small rivers, where a number of glacial and landslide deposits are found.

2.1. Geological framework

The rockslide studied in this paper is part of the La Engorda landslide complex, a group of rock avalanches, rock slides, rock falls, and solifluxion deposits, stratigraphically placed on top of three levels of moraine deposits (Gonzalez, 2010). Rock avalanche deposits of volume over 10^6 m^3 dominate the area, highlighting four major events, whereas the slopes that surround the complex show distinct smaller planar rock slides, one of which is studied here. The studied rock slope belongs to the Río Damas Formation [defined by Klohn, 2015, in the Damas River Valley, in the Province of Colchagua (35°S), as a complex of fine and coarse clastic sediments, as well as of sporadic chemical sediments], which is characterized by a thick sequence (3000–4000 m) of Jurassic red continental detrital and volcanic rocks with vertical bedding (Charrier et al., 2002; Rossel et al., 2014). The lower Formation contains abundant volcanic breccia of various block sizes, whereas the upper part contains intercalated andesitic basaltic lava flows. The sediments mostly exhibit continental origin, such as fluvial, eolian, alluvial, and lake environments (Rossel et al., 2014). The formation is concordant with the Rio Colina formation at its base and with the Lo Valdés formation at its roof. The sedimentary beds of the Río Damas Formation represent the Upper Jurassic (Kimmeridgian) continental back-arc deposits, cropping out in the Principal Cordillera of central Chile and Argentina, respectively (Fock, 2005).

Rock samples gathered from the rockslide area indicate that the main lithology is a coarse conglomerate composed of volcanic and

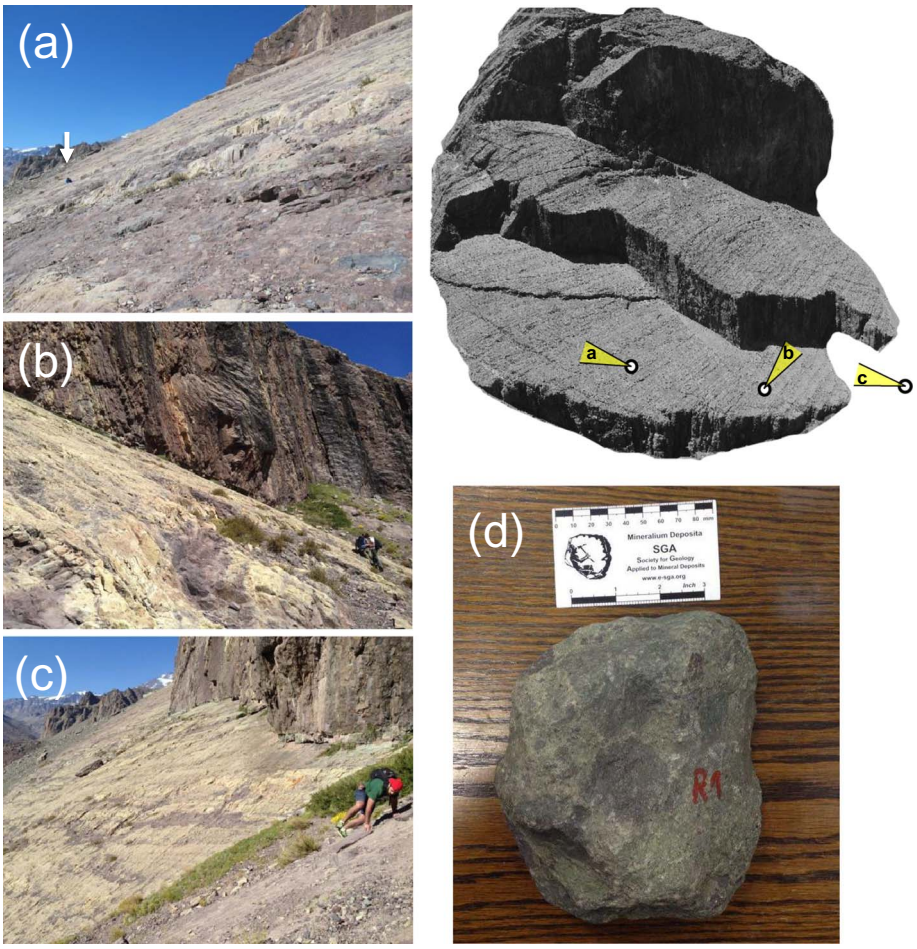

Fig. 2. Views of the rock slope. (a) to (c) Different views of the first bedding plane. The arrow indicates the location of people on the slope as scale. (d) Rock sample from the rock slope.

terrigenic clastic fragments supported by a fine-grained sedimentary matrix. The clasts and the matrix show a strong pervasive alteration, exhibiting chloritization and an advanced weathering degree (Fig. 2). Clasts sizes range between 1 and 5 cm, and the dominant families fall in the range 3–4 cm. A number of igneous dykes and sills, of dominant felsic composition, can be seen at the first sliding step, near the NW slope edge (Fig. 1b). The samples also show a strong propylitic alteration, similar to the enclosing rock, and a similar degree of weathering. The dyke swarm showed a finer grain size than the host rock.

2.2. Seismological framework

Most of the geomorphologic regional features in the territory of Central Chile were formed due to the subduction of the Nazca plate underneath the South-American plate (Farías et al., 2010). As a consequence, four seismogenic zones can be identified: the outer-rise seismic zone associated to the stress of the Nazca flexural motion, the interplate seismic zone associated to the relative motion in the plates contact, the intermediate-depth intraplate seismic zone, dominated by tensile fractures of the Nazca plate, and the shallow-intraplate seismic zone in the overriding South American plate at depths lower than 30 km (Leyton et al., 2010).

Fig. 3 shows the seismic activity recorded in Central Chile from 1950 to 2018, considering earthquakes with moment magnitude larger than Mw 4.0 (data downloaded from the USGS's Earthquake Catalog database https://earthquake.usgs.gov, last accessed January 2018). Crustal seismic activity in the High Andes Cordillera region correlates with variations in the subduction dip angle of the Nazca plate, which transitions from flat in the north of the 33°S to an angle of nearly 27° in the south (Alvarado et al., 2009; Pardo et al., 2002). The seismic activity between 33 and 35°S is distributed mainly along the western flank of the Andean mountain chain. Although the largest activity is concentrated in the upper Maipo and Cachapoal Rivers, there is also concentrated activity in Las Melosas and the San José volcano near the studied area (Barrientos et al., 2004). Barrientos et al. (2004) also identified seismic activity associated to the Pocuro fault, the Olivares River, and in the north of Tupungatito Volcano that may not be relevant for this study given the pronounced attenuation of shallow crustal earthquakes (Sadigh et al., 1997).

Historical seismic activity has been observed in the Maipo Valley in 1850, 1870–1880, 1905 and 1947 (Flores et al., 1960). The 1850 earthquake, with an estimated magnitude between 7 and 7.5, killed two people and caused large rockslides 14 km south of the San José de Maipo town (Lomnitz, 1970). A sequence of earthquakes started in August 28, 1958 in the upper Maipo Valley, culminating with three large events occurred on September 4, 1958, the largest of which, known as Las Melosas earthquake (epicenter shown in Fig. 1a), had an estimated moment magnitude Mw = 6.3, a focal depth of about 8 km, and a strike-slip focal mechanism (Alvarado et al., 2009). This earthquake caused intensities as high as 9 in the MSK scale, peak horizontal accelerations in the order of 1 g, and Arias intensities of about 11.5 m/s (Sepulveda et al., 2008). More recently, crustal earthquakes near the Chile-Argentina boundary have been recorded in 1987 (Mw = 5.9), 2001 (Mw = 5.1), and 2004 (Mw = 6.5) (Alvarado et al., 2005, 2009).

Assessments by Pérez et al. (2014) confirmed that most of the seismic activity is located near the Chile-Argentina boundary, aligned with the El Fierro Fault system, and that the crustal seismicity trends in the N–S direction, following a series of folds and faults that dominate

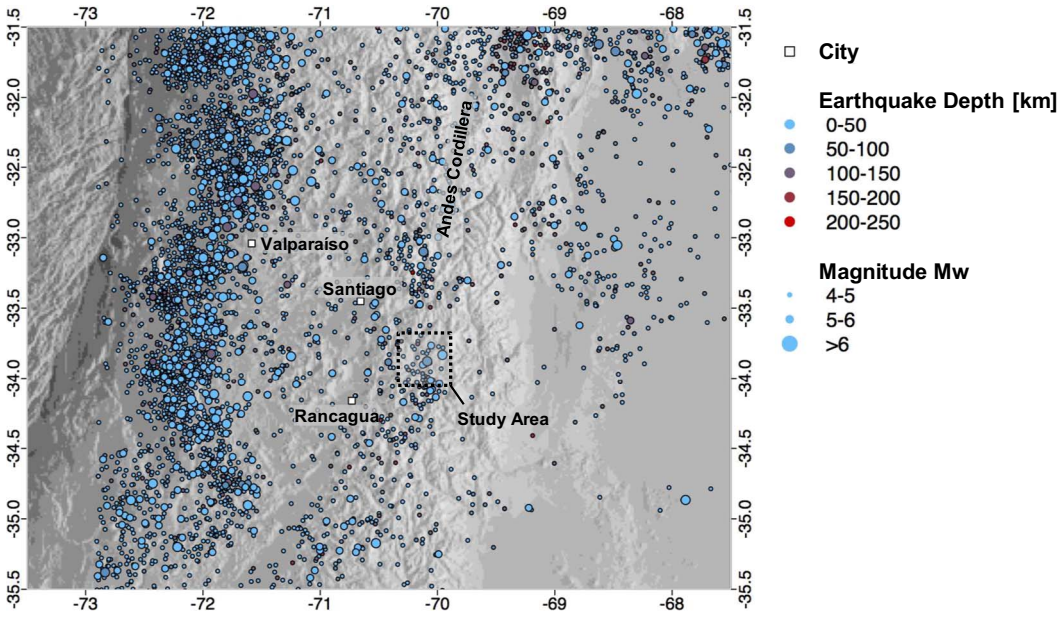

Fig. 3. Seismic activity recorded in Central Chile from 1950 to 2018. The data considers earthquakes with moment magnitude larger than Mw 4.0 (data downloaded from the USGS's Earthquake Catalog database https://earthquake.usgs.gov, last accessed January 2018).

the region (Fig. 1a). In fact, the Chacayes-Yesillo and the Diablo regional west-vergent thrust faults crop out and fault-propagating folds (Fock, 2005) deform the rocks around the point identified as the Las Melosas earthquake epicenter (Sepulveda et al., 2008). The presence of such blind faults near the surface may contribute to the rupture process of shallow crustal earthquakes in the region.

3. Development of the numerical model

3.1. Rock slope geometry

The exposed surfaces of the rockslide were scanned by Sepúlveda et al. (2012) in a wide area across the sloping terrain using an Optech ILRIS-3D ER terrestrial laser scanner, which produced 35 topographic profiles from the foothill to the main scarp. The scanning comprised 7.9 million points and resulted in an approximate resolution of one point per 12 cm on the slide scar. Fig. 4 shows the LIDAR profiles aligned in the dip direction (N47°W). The two bedding planes and the two steps observed at the site are best represented by the 2D profiles in the center of the rock slope. In particular, Fig. 4 highlights the most representative profile adopted for the two-dimensional numerical model. The measured orientations of the bottom and top sliding surfaces are (dip direction/dip angle) 314°/35° and 314°/40°, respectively.

In order to reconstruct the geometry of the hill before the rock slope failure, the individual surfaces of the chosen profile were simplified using a first order equation and joined at the intersection points. The main scarp and the first footwall were extrapolated to define the original rock slope. From the main scarp, the surface through the mount top and the back-slope was reconstructed using LANDSAT imagery and DEM rasters. The scarp was projected as a straight line, disregarding erosive effects due to the low impact on the landslide volume. DEM imagery shows slight changes along the projected plane from the lower ramp to the deposit cone. Fig. 5 shows the final model geometry with the adopted rock slope profile and the reconstructed, simplified 2D hill geometry. The projected structural data of the discarded minor joint-sets over the selected profile (36°, 82°, and 83°) matches the exposed surfaces of the sliding planes.

In order to validate the reconstructed rock slope geometry adopted

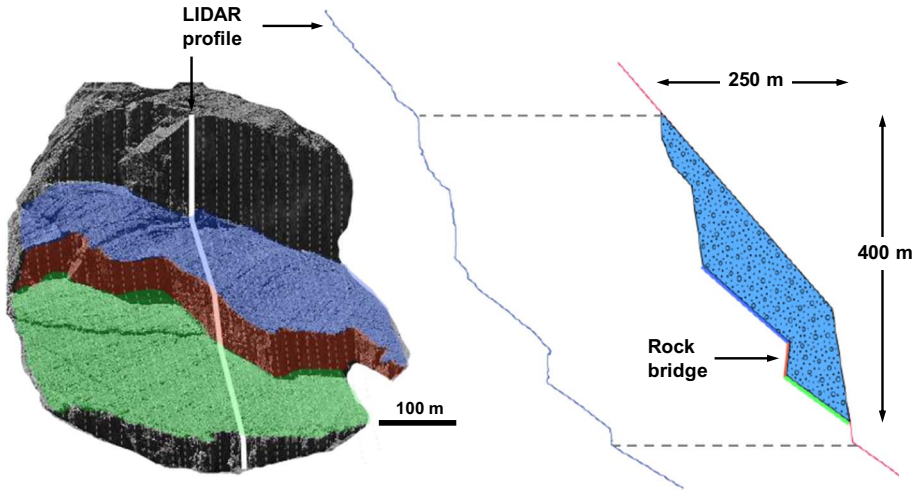

Fig. 4. Reconstruction of a representative section of the original rock slope geometry. The white thick line in the slope is the location of the selected LIDAR profile. The model on the right is the reconstructed original geometry of the 2D section.

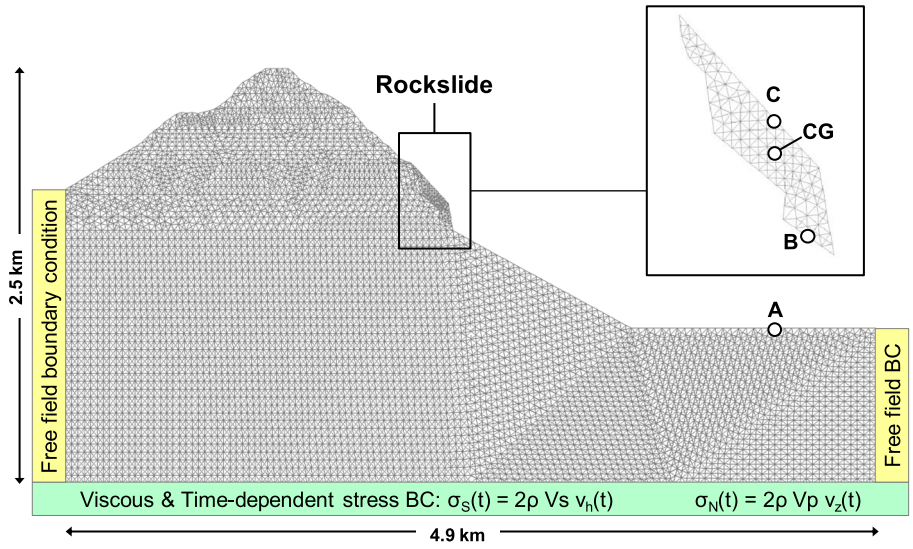

Fig. 5. Numerical model of the rock slope analyzed with the UDEC® software. The point CG indicates the position of the center of gravity of the failed rock slope section reconstructed in Fig. 4. Points A, B, and C are control points used in the analysis.

in this study, we compared an estimate of the reconstructed rock slide volume with the total volume of the deposit. Projecting the 2D rock slope profile over an average width of 430 m (measured with satellite imagery), the reconstructed rockslide volume is 10 Mm^3. On the other hand, the size of the rockslide deposit was estimated from information collected during a field survey. The extent of the removed material runs from the foothill to the riverbed, covering the area across a local road (Fig. 1c). LANDSAT images were used to support the mapping and the entire deposit area was estimated at 0.63 km^2. The deposit depth was difficult to estimate due to the lack of a stratigraphic columns and open cuts in the field, but considering the exposed deposit areas adjacent to the local road, the average deposit depth can be estimated in the order of 10 m. Since adjacent alluvial cones covered lateral portions of the rockslide, hindering the exact deposit extent, the real volume can be considered 30% to 50% larger, based on imagery analysis. Hence, the total volume of the deposit would be consistent with the volume calculated for the rock slope. This first order estimation of the volume assumes that bulking, which can range between 20 and 30% (Sturzenegger and Stead, 2012), may be canceled out due to erosion from the Volcan River (Fig. 1b).

Table 1
Rock mass and joint mechanical properties.

Property	Units	Value
Rock mass		
Density, ρ_r	kg/m^3	2750
Young's modulus, E_r	GPa	35
Poisson's ratio, ν_r	–	0.2
Bulk modulus[a], K_r	GPa	19.4
Shear Modulus[a], G_r	GPa	14.6
Internal friction angle, φ	°	53
Cohesion, c	MPa	15
Tensile strength, σ_t	MPa	11.8
Joints		
Joint compressive strength, JCS	MPa	120
Joint roughness coefficient, JRC	–	4
Residual internal friction, φ_r	°	33
Normal stiffness, J_{kn}	GPa/m	10
Shear stiffness, J_{ks}	GPa/m	10

Note: All the tests were conducted in the Block Caving Laboratory at the Mining Engineering Department, University of Chile.
[a] Calculated from elastic relationships from the Young's modulus and the Poisson's ratio.

3.2. Mechanical properties

Mechanical properties of the rock mass were obtained from samples collected at the slope. The rock mass was considered as homogeneous with the presence of joints. Three different blocks were sampled in order to reflect the grain-size variation, the minimum weathering level, and the mineralogy observed in the in-situ rock. One sample with coarse grain size was taken from the main sliding surface (UG1), and two additional samples (UG2, UG3) were tested in order to estimate the variability of the properties. Table 1 shows the rock density ρ_r, the Young's modulus E_r, and the Poisson's ratio ν, based on tests results from sample UG1. The experimental program also considered triaxial, uniaxial, and Brazilian tests to estimate rock strength parameters (Table 1). These parameters were integrated into an elastic-perfectly plastic Mohr-Coulomb constitutive model for the rock mass.

The main joints that form the sliding planes were assumed as open-joint systems since no evidence of gauging was found. In addition, three minor closed-joint sets were identified in the slope, whose orientation records were collected during two field campaigns. These minor joint sets did not affect the global stability of the rock slope, which was evidently controlled by the planar structures that form the bedding planes (open joints with almost no cohesive strength). On the other hand, the field mapping reported a very low spacing (3–5 cm) at the first bedding plane and both steps. A seismic signal analysis of the selected input earthquakes in this study showed a reduced range of dominant frequencies (between 0.2 and 4.5 Hz), which combined with the shear wave velocity calculated for the tested sample (~2300 m/s) would have negligible impact over the shear stress generated between the minor joints due to the long wavelengths developed through the rock slope (the shortest wavelengths are in the order of 500 m). These facts allowed the discarding of the three minor joint sets, leaving only the main joints that separate the rockslide from the slope, greatly simplifying the model and the analysis.

The Barton-Bandis constitutive model was adopted for the main joints described above. The model defines the maximum shear strength τ [Pa] as a function of the normal stress σ_n [Pa], the joint roughness coefficient JRC [-], the joint compressive strength JCS [Pa], and the residual friction angle φ_r [°] (Barton, 1982)

$$\tau = \sigma_n \tan\left[\mathrm{JRC}\ \log\left(\frac{\mathrm{JCS}}{\sigma_n}\right) + \phi_r\right] \quad (1)$$

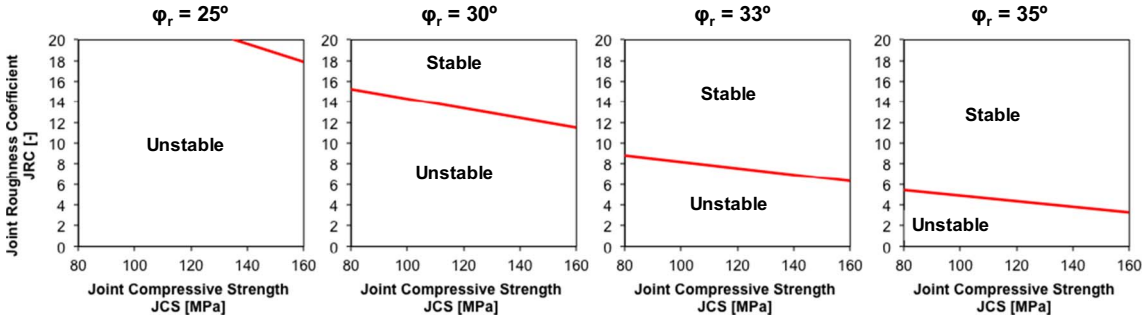

Fig. 6. Static stability chart of the rock slope without rock-bridge. Each box corresponds to a different residual friction angle φ_r of the bedding plane in Fig. 2c.

The residual friction angle is estimated at $\phi_r = 33^\circ$. Sepúlveda et al. (2012) performed several Schmidt Hammer field tests to estimate the most representative joint wall compressive strength as JCS = 120 MPa.

Variability in the estimation of JRC based on digitized rock surfaces (Alameda-Hernández et al., 2014) and scale-effects in the joint shear strength (Bahaaddini et al., 2014; Hencher and Richards, 2015) complicate the adoption of a JRC for large sliding planes. Due to these two effects, as well as to compensate for loss of accuracy when representing a 3D surface with a single 2D profile (e.g., null supporting confining stress in the out-of-plane horizontal direction), the JRC was studied under static conditions in a following section in order to improve the estimation of the original sliding-planes resistance.

3.3. Model boundary conditions

The model boundary conditions were defined to consider dynamic input motions at the model base. Nonetheless, the same boundary conditions apply for static analyses. Free-field boundary conditions were applied at both right and left model boundaries to emulate an infinite region, and viscous boundaries were applied at the bottom of the model (in both x and y directions) to reduce seismic wave reflection (Gischig et al., 2015; Itasca, 2016; Luo et al., 2012). Viscous boundary conditions were applied in terms of stress, considering the intact rock elastic properties (i.e., density, bulk modulus and shear modulus, which are shown Table 1). Using the rock density, the Young's modulus, and the Poisson's ratio (Table 1), the compressive and shear wave velocities were estimated as Vp = 3760 m/s and Vs = 2300 m/s, respectively. The applied mesh considered a maximum element size of 50 m for the base and 25 m for the rock slope (Fig. 5) in order to capture 1/12 to 1/8 of the shortest wavelength for a maximum frequency of 4.6 and 9.2 Hz in the base and the slope (Chen and Zhao, 1998), which coincide with the relevant frequencies of the input signals. All model parts were meshed with triangular edge shapes to discretize the irregular geometry of the mount summit. In addition, a distance of 1500 m was added at each side and to the bottom of the rock slope to prevent numerical boundary effects, resulting in a model of 2.5 km height and 4.9 km width (Fig. 5).

Local damping proportional to each element total stress was used for the static analysis. This particular damping shows the best time-precision ratio according to Itasca (2016) documentation for static analyses. For the dynamic simulations, Rayleigh damping was introduced using a mass matrix constant α and a stiffness matrix constant β. The associated minimum damping angular frequency and the minimum critical damping ratio are defined as $\omega_{min} = (\alpha/\beta)^{1/2}$ and $\xi_{min} = (\alpha \cdot \beta)^{1/2}$, respectively. The parameters α and β can be expressed in terms of the minimum and maximum frequencies of interest, f_i and f_j [Hz], respectively, as

$$\alpha = \frac{4\pi\xi f_i f_j}{f_i + f_j} \quad (2)$$

$$\beta = \frac{\xi}{\pi(f_i + f_j)} \quad (3)$$

The extreme frequencies were set to $f_i = 1$ Hz and $f_j = 5$ Hz and the fraction of the critical damping was chosen at $\xi_{min} = 0.01$, which are consistent with the seismic records dominant frequencies that range between 0.2 and 4.5 Hz. The adopted critical damping value limits accelerations in the rock slope that would be unrealistically high otherwise.

4. Rock slope static stability

A sensitivity analysis was performed to evaluate the impact of the joint properties, JCS, JRC, and φ_r, on the slope static stability when the entire sliding surface is considered purely frictional, i.e., the joints between the base and the sliding rock mass are opened. The need for this analysis is to account for the variability of these properties along the sliding surfaces. The domains of these variables were chosen from the parameters obtained in the laboratory, the field inspection, and values from the literature. JCS values ranging between 80 and 160 MPa, JRC between 1 and 20 and φ_r between 25° and 35° were tested. Spatial variability of the rock mass properties throughout the model was disregarded despite the model size, and the constant rock mass properties in Table 1 were adopted.

Fig. 6 shows stability charts for different joint residual friction angles (φ_r = 25° to 35°) as a function of the JCS and JRC. The diagrams indicate the combination of JCS and JRC values that result in static stable/unstable rock slope states. The static stability of the rock slope is very sensitive to the JRC and φr, but less sensitive to the JCS value. The rock slope is statically unstable for a wide range of JRC values; for example, if a residual friction angle φr = 33° and JCS = 120 MPa are considered, the rock slope is unstable for JRC values between 1 and 7, which is consistent with the global roughness of the sliding plane shown in Fig. 2c and the LIDAR profile in Fig. 4. This result suggests that it is unlikely that the rock slope was able to stand under static conditions by only frictional strength along the exposed sliding surfaces. Hence, the presence of at least one rock-bridge is required for the rock slope to be statically stable. In such case, the model would be statically stable for all the tested variable ranges. Considering the field campaign observations used to improve the LIDAR measurement's precision on the surface, along with the discussed static stability analysis, we adopted the average value JRC = 4 (the average JRC value in the unstable zone in the plot for φr = 33° and JCS = 120 MPa) for the following dynamic analyses.

5. Rock slope dynamic response

The rock slope dynamic analysis comprised the application of seismic records in the base of the model (Fig. 5). The earthquake records were input as shear stress $\sigma_s(t)$ [Pa], in order to be consistent with the viscous boundary condition (Gischig et al., 2015; Itasca, 2016), as a function of the instantaneous tangential velocity at the base $v_s(t)$ [m/s],

the rock shear wave velocity Vs [m/s] and the rock density ρ [kg/m^3]

$$\sigma_s(t) = 2\rho V_s v_s(t) \quad (4)$$

The instantaneous tangential velocity was calculated from integration of the acceleration records. The adopted rock mass and joint properties for the dynamic analysis are shown in Table 1.

In the absence of available seismic records from the area of interest, we evaluated the slope seismic behavior using records from historical shallow crustal earthquakes, such as the Northridge (1994), the Chi Chi (1999) and the Kobe (1995) earthquakes, understanding that these records have different frequency contents, Arias intensities, peak ground accelerations and velocities, distances to the rupture area, as well as durations (similar approach is adopted in Gischig et al., 2016). All the records were downloaded from The PEER Ground Motion Database at the University of California, Berkeley (see http://ngawest2.berkeley.edu, last visited in August 2017). In this context, the response of the rock slope is explored with a broader set of input motions. We disregarded thrust earthquake records since the attenuation of seismic waves at distances larger than 150 km from the rupture area reduces considerably the surface intensities (Contreras and Boroschek, 2012; Idini et al., 2017; Montalva et al., 2017).

The dynamic analysis only considered acceleration time histories recorded in stations with shear wave velocities of the upper 30 m Vs_{30} larger than 250 m/s to avoid local site effects induced in flexible soil deposits that can modify the amplitude and frequency content of the strong motions expected in the surface of stiff soils and rock outcrops. Table S1 in the Supplementary material summarizes the main characteristics of the earthquake records, including the duration, the Arias Intensity, the peak ground velocity (PGV), the peak ground acceleration (PGA), the peak frequency of the Fourier spectrum, and the site shear wave velocity of the shallower 30 m at the station, Vs_{30}. The peak accelerations of the 100 input records in the base of the model ranged between 0.03 and 0.96 g, their durations between 25 and 167 s, their Arias intensity between 0.02 and 7.7 m/s, and their peak frequency between 0.2 and 4.8 Hz. Fig. 7 shows the relationship between the Arias Intensity, the peak horizontal acceleration, the duration, and the Fourier spectrum peak frequency of the selected records for each of the three earthquakes. While there is a strong correlation between the Arias Intensity and the peak horizontal acceleration, no correlation was found between the other variables of the records. Note that, we should at least have halved the input motions if the site conditions where the accelerations were recorded wanted to be reproduced. However, since we were not interested in the reproducing the site conditions of the records and this study focuses on testing the rock slope response subjected to a wide range of maximum accelerations, Arias Intensities, frequency content, and duration, no such correction was performed.

The Fourier spectra of the input signals show important energy content at low frequencies (Fig. 7b); Northridge earthquake records have peak frequencies in the range 0.8–4.5 Hz, Chichi records between 0.2 and 4.8 Hz, and Kobe records between 0.5 and 3 Hz.

In what follows, point A in Fig. 5 will be considered as a reference for ground motion amplification. We verified that the amplification in this point follows the one-dimensional amplification factor with respect to the bottom of the model, defined by the 1D shear wave propagation theory. The point was selected as a free field measure since boundary and topographic effects are minimized. Fig. 8 shows the peak ground accelerations calculated in point A as a function of the peak acceleration in the input motion. The trend in the figure shows that the peak acceleration at the surface more than doubles the input peak acceleration as the seismic waves approach to the model surface, reaching values as high as 1.32 g (input record LDM-064), slightly larger than the PGA recorded at the PUL station (component oriented with a 194° azimuth) for the 1994 Northridge earthquake (Sepúlveda et al., 2005).

In addition to the surface amplification of the input ground motions, the numerical model predicts large amplifications in terms of peak accelerations in the surface of the sliding rock slope (point C in Fig. 5). Point C was chosen as a measure of topographic amplification on the surface of the rock slope with respect to the reference point A. The trend in Fig. 8b shows that peak acceleration in the block surface more than doubles that calculated at the model surface (point A in Fig. 5); values ranging between 0.1 and 2.34 g were calculated (the highest acceleration corresponds to the input record TAZ-090). These large accelerations are consistent with international seismic site classification codes that recommend amplifying by a factor of two to account for topographic amplification (e.g., Eurocode 7) and reasonable if no material damping is adopted.

As the seismic waves amplify from the input record to the model surface and the rock slope, relative displacements along the sliding surface (point B in Fig. 5) are recorded.

Point B was selected at the contact of the rock block with the sliding surface, where the relative displacement between the block and the base was along the plane. We verified that logging points above the interface include rotation and other non-linear movements once the rockslide starts to detach and fall from the mountain. Fig. 9 shows an example of the rock slope behavior when a seismic record of the Chi Chi earthquake in the CHY006 station is the input of the numerical model (Fig. 9a). The seismic waves amplify at the model surface (Fig. 9b) and subsequently at the rock block center of gravity shown as CG in Fig. 5 (Fig. 9c), resulting in a total accumulated rockslide relative displacement calculated in the point B of 6 m after 25 s of strong shaking (Fig. 9d). On the other hand, Fig. 9 also shows the response of the rock slope when a different seismic record of the Chi Chi earthquake (WNT station) is the input of the numerical model. In this case, the rockslide displacement continuously increases until reaching a large displacement in the order of 30 m (Fig. 9h).

The rockslide relative coseismic displacement along the sliding

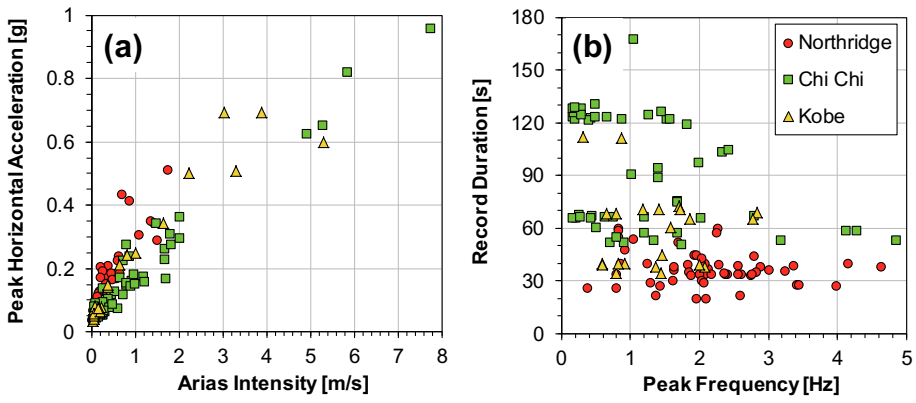

Fig. 7. Parameters of the input records from the Northridge, Chi Chi, and Kobe earthquakes used in this study.

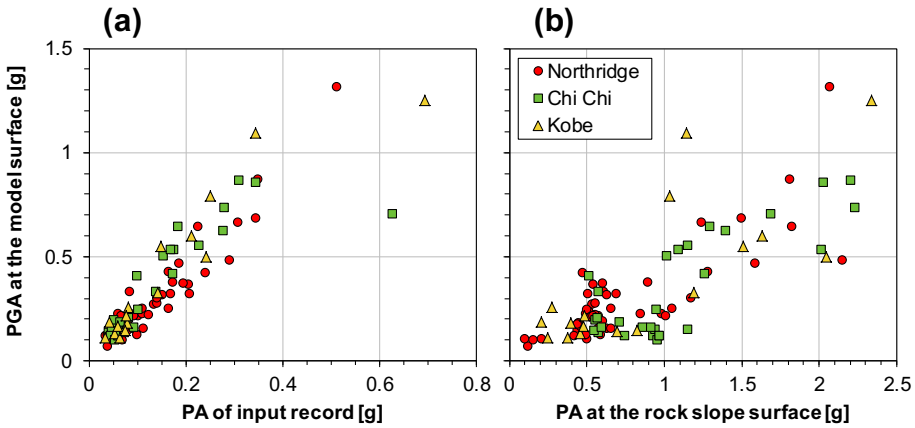

Fig. 8. Peak accelerations calculated by the numerical model. (a) Relationship between the peak acceleration (PA) of the input record and the peak ground acceleration (PGA) at the model surface in the point A (Fig. 5), and (b) relationship between PGA and the peak acceleration calculated in the rock slope surface (point C in Fig. 5).

surface can be correlated with parameters calculated in the rockslide center of gravity (CG in Fig. 5), such as the peak acceleration, the Arias Intensity, the significant duration, the peak velocity, and the peak frequency of the acceleration time histories. The best correlation with the displacement was found to be the peak velocity (correlation coefficient cc = 0.914), followed by the Arias Intensity (cc = 0.875), and the peak acceleration (cc = 0.852) (Fig. 10); the peak frequency of the acceleration input record, as well as the peak frequency of the acceleration time history and the significant duration calculated at the center of gravity (CG in Fig. 5) exhibit poor correlation with the displacement (Fig. 11). High correlation with the peak velocity has also been found for earthquake damage (Wu et al., 2003) and earthquake-induced landslides (Wang et al., 2010). Note that the rockslide relative displacements in Figs. 10 and 11 were limited to 60 m because larger displacements over the sliding plane correspond to detachment of the rock block from the mount, and the numerical model cannot accurately predict such highly nonlinear behaviors.

The resulting seismically induced rock slope behavior was classified into 3 groups, according to the displacement over the sliding surface:

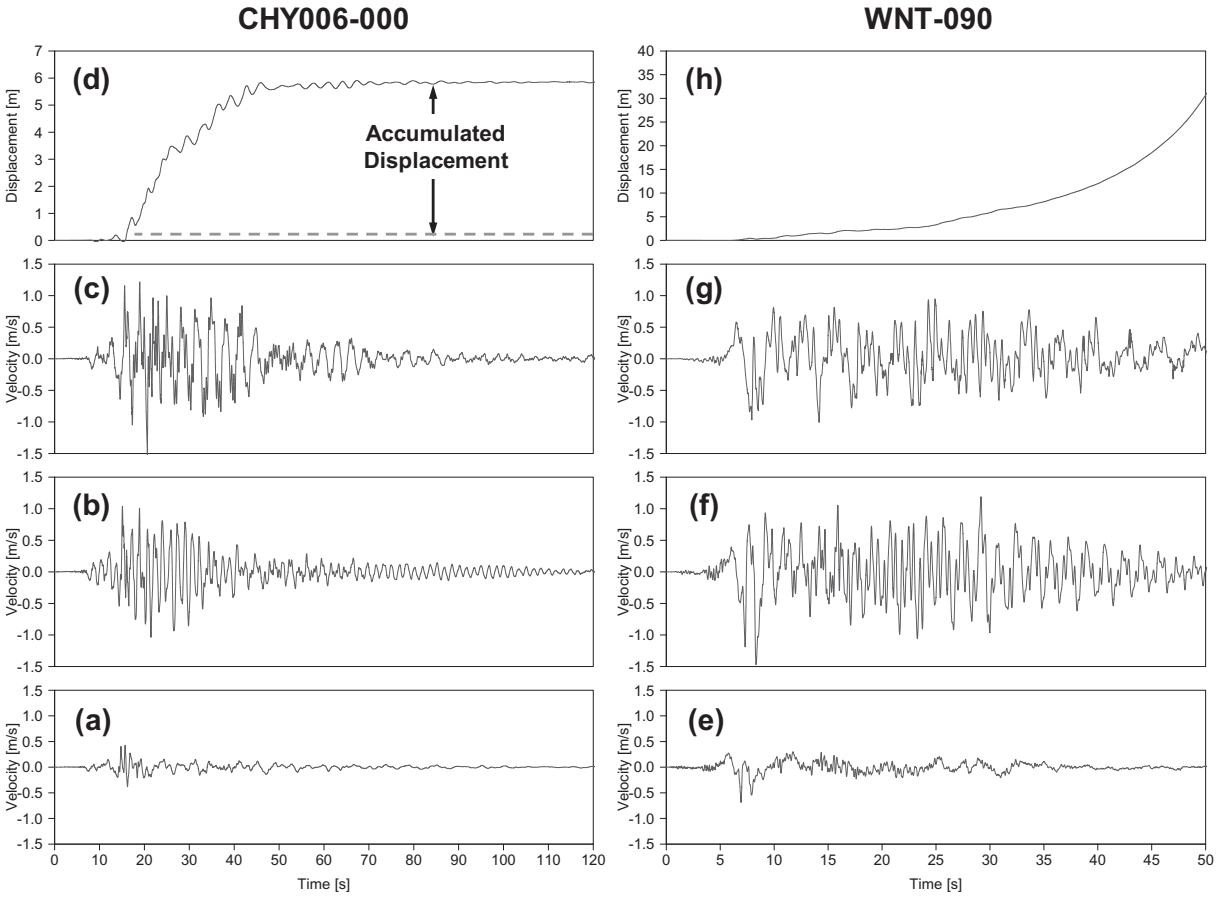

Fig. 9. Velocities and relative displacements of the rock slope when subjected to velocity records of the Chi Chi earthquake (stations CHY006 and WNT). (a) and (e) are the input velocities in the model base, (b) and (f) are the velocities calculated at the model surface, (c) and (g) are the velocities calculated in the rock slope center of gravity, and (d) and (h) are the rock slope relative displacements.

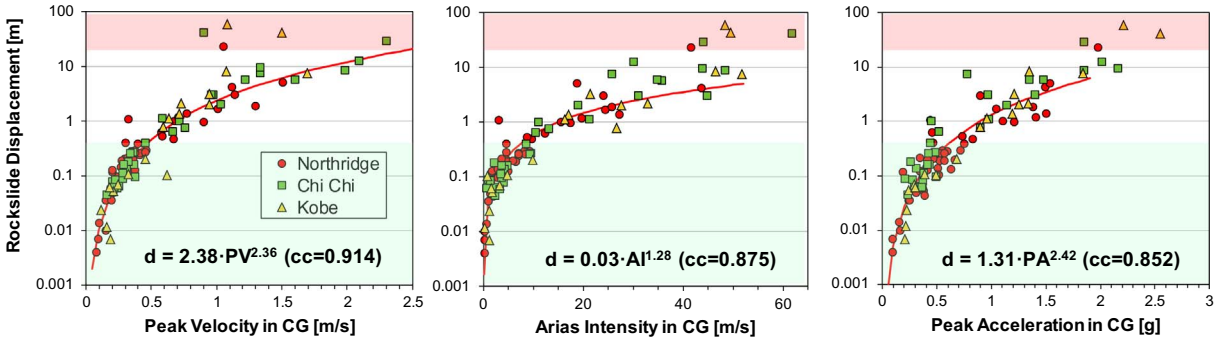

Fig. 10. Rockslide displacement as a function of the peak velocity, the Arias Intensity, and the peak acceleration calculated in the rock slope center of gravity for the 100 seismic records of the Northridge, Chi Chi, and Kobe earthquakes. The green shaded area represents no-failure and the red shaded area complete failure. The correlation coefficients (cc) are shown in parentheses. (For interpretation of the references to colour in this figure legend, the reader is referred to the web version of this article.)

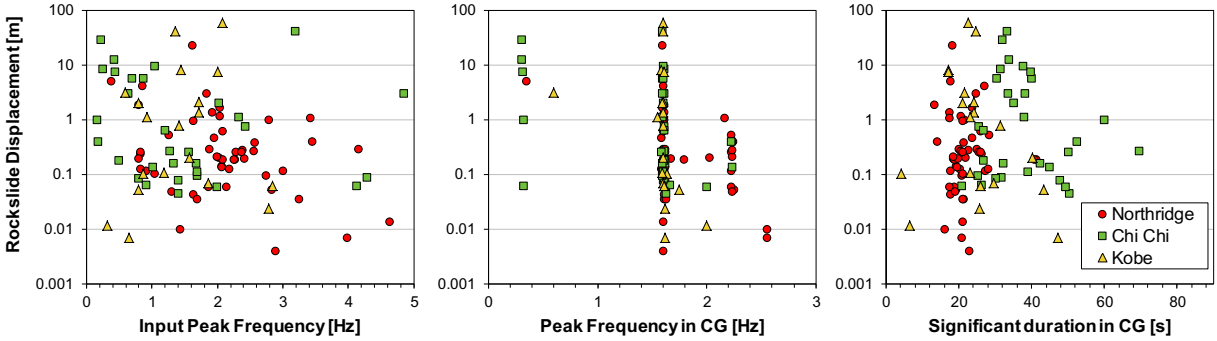

Fig. 11. Rockslide displacement as a function of the peak frequency of the acceleration input record, as well as the peak frequency of the acceleration time history and the significant duration calculated at the center of gravity for the 100 seismic records of the Northridge, Chi Chi, and Kobe earthquakes.

- No-failure: Small sliding along the surface compared to the surface length. The logged displacement does not accumulate over time. Simulations with relative displacements below 0.5 m fall into this category.
- Limited Failure: This failure mode shows incremental sliding, followed by a rock-mass stabilization with relative displacements between 0.5 and 20 m (e.g., CHY006 record response in Fig. 9).
- Complete Failure: This failure mode shows a continuous incremental displacement over the surface, leading to a complete slope failure and triggering of the rockslide. Simulations with displacement above 20 m are included in this category (e.g., WNT record response in Fig. 9). Beyond this threshold, most of the failed material reaches the border of the sliding plane, turning into a complex non-linear and rotational motion; hence, the rockslide displacement does not exactly follow the direction of the sliding surface.

Fig. 12 shows examples of the predicted rock slope for both failure types after the earthquake record is applied in the model. In the cases of "limited failure", there is a partial failure of the rock bridge, whereas in the "complete failure" case, there is massive tensile failure in the slope. The trends depicted in the Fig. 10 only consider cases in which no-failure and limited-failure were predicted. Cases with complete failure were disregarded because the relative displacement continuously increases beyond the total duration of the input ground motion (e.g., WNT record response in Fig. 9). It can be anticipated that when the rock slope is affected by limited failure, it can eventually fail under the repetitive action of earthquakes that can incrementally deteriorate the rock slope.

Fig. 13 shows the rockslide relative displacement as a function of the peak velocity, the Arias Intensity, and the peak acceleration at the model surface in point A (Fig. 5). Although the correlation with respect to the variables in the rockslide center of gravity decreases (Fig. 10), the trends still prevail and indicate that peak accelerations larger than

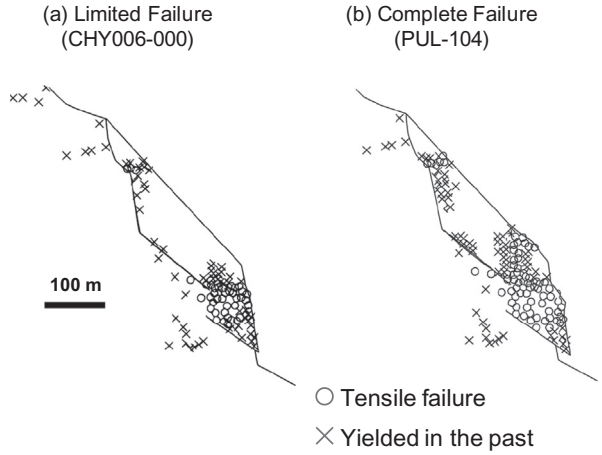

Fig. 12. Damage pattern of the rock slope when subjected to an earthquake record. (a) Limited failure (displacement along the bedding plane lower than 20 m) and (b) complete failure (displacement along the bedding plane larger than 20 m). Yielded in the past corresponds to elements that no longer satisfy the Mohr-Coulomb yield criterion.

0.3 g, Arias Intensities larger than 5 m/s, and peak velocities larger than 0.4 m/s in the free field can cause limited failure in the rock slope. In addition, free field peak accelerations of 0.6 g, Arias Intensities of 8 m/s, and peak velocities of 0.6 m/s are lower bounds of complete rock slope failure.

Acceleration time histories recorded at the same stations in perpendicular directions, very similar in amplitude and frequency content, can cause different rock slope response. For example, the rockslide displacement corresponding to the Northridge earthquake record at the station CHL vary from 1 m to 22 m total displacement despite having similar input peak accelerations in both directions. Similar results are

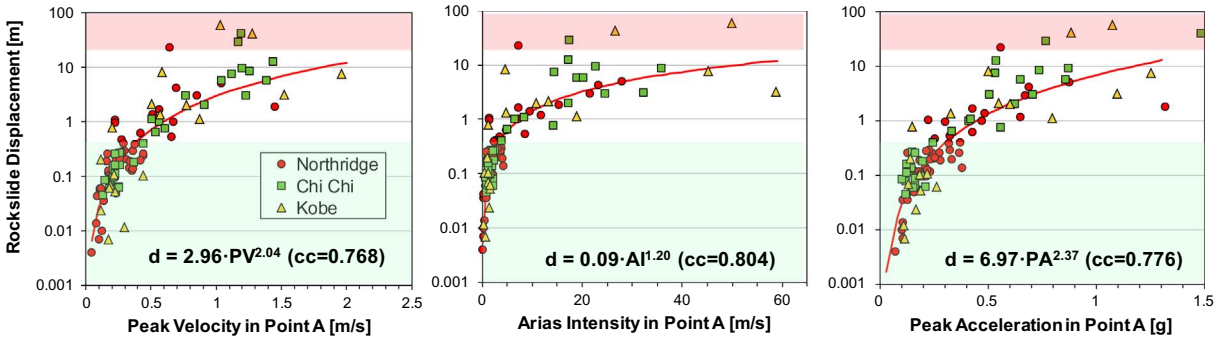

Fig. 13. Rockslide displacement as a function of the peak velocity, the Arias Intensity, and the peak acceleration calculated at the model surface (point A in Fig. 5) for 100 seismic records of the Northridge, Chi Chi, and Kobe earthquakes. The green shaded area represents no-failure and the red shaded area complete failure. The correlation coefficients (cc) are shown in parentheses. (For interpretation of the references to colour in this figure legend, the reader is referred to the web version of this article.)

found for records in the PUL, ALS, CHY006, CHY029, TCU102, WNT and TAZ stations, where the displacement significantly differs between components.

In order to test whether the polarity of the input signal can affect the rock slope response and the magnitude of the relative displacements, records from Northridge earthquake were input with a reverse polarity. However, no systematic change in the correlation shown in Fig. 10 and change in the type of failure were found.

5.1. Rock slope dynamic response to bi-directional input acceleration

In addition to the horizontal acceleration, we computed the sensitivity of the slope response to the combination of horizontal and vertical accelerations. The analysis was performed subjecting the model to the horizontal and the vertical components of the record in the same stations analyzed in the previous section, logging the displacement in the same control points (Fig. 5). The peak vertical accelerations of the records considered in this analysis are shown as a function of the horizontal peak accelerations in Fig. 14a. Despite few records from the Chi Chi earthquake, the horizontal peak accelerations are larger than the vertical ones.

Fig. 14b shows the relationship between the rockslide displacements when the horizontal and vertical components are inputs in the numerical model as a function of the displacement obtained from the horizontal input only. The addition of the vertical component slightly increases the displacement along the sliding surface, but it does not change the failure mode. Few cases that result from inputs of the Northridge earthquake reduce their displacements when subjected to bi-directional ground motions, whereas all the simulations for input peak vertical accelerations larger than horizontal ones show an increase in the displacement. This result is relevant since large vertical accelerations are expected from shallow crustal earthquakes in the Maipo river valley (Flores et al., 1960; Sepulveda et al., 2008).

6. Discussion

The results show a good correlation between the rockslide relative displacement and the peak velocity, the Arias Intensity, and the peak acceleration. This result suggests that pseudo static analyses with a seismic coefficient proportional to the maximum acceleration could be appropriate to analyze the dynamic behavior of the rock slope.

We compared the frequency content of the three sets of records with the vibration modes of the numerical model. Recall that the Northridge earthquake records have peak frequencies in the range 0.8–4.5 Hz, Chichi records between 0.2 and 4.8 Hz, and Kobe records between 0.5 and 3 Hz (Fig. 7b). Simulations of the three earthquakes show distinctive peak frequencies in the center of gravity of the rockslide clustered at 0.3, 1.6, and 2.2 Hz (Fig. 11). An eigenvalue analysis of the model shows that the fundamental vibration mode of the model is 0.3 Hz. Although this frequency is excited by some of the records of the Chi-Chi earthquake (Fig. 11), the rockslide does not seem to respond with a higher displacement.

Large thrust earthquakes occur in Central Chile every 80 years, approximately (Udias et al., 2012), affecting the rock slope stability in addition to shallow crustal earthquakes. However, thrust earthquakes do not pose significant risk in the area of the rockslide due to the pronounced attenuation of the seismic waves. For example, the Mw 8.8 El Maule 2010 earthquake with a hypocentral depth of 28.8 km and a rupture area of 61,000 km^2, can cause at 150 km, the distance from the earthquake rupture area to the rock slope, PGAs of 0.13 g, 0.16 g and 0.08 g, using the Contreras and Boroschek (2012), Idini et al. (2017) and Montalva et al. (2017) ground motion prediction equations for

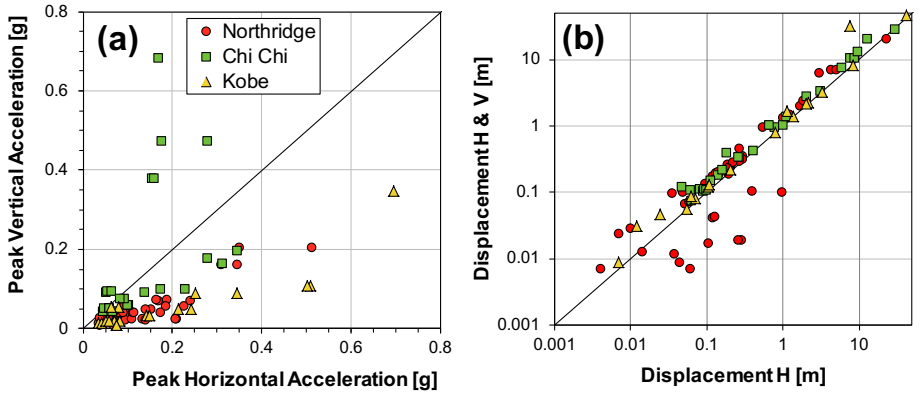

Fig. 14. Effect of bidirectional input motion in the numerical model. (a) Peak vertical acceleration as a function of the peak horizontal acceleration in the input of the model and (b) rockslide displacement along the sliding plane when bidirection input is considered (H & V) as a function of the rockslide displacement for horizontal input only (H).

interplate subduction earthquakes. According to our results, these small peak accelerations in the free field result in limited relative displacements (Fig. 13). In contrast, regional scale studies of large volume paleolandslides in the Andes Main Range of Central Chile, suggest a close geographic relationship between landslides and active faults (Antinao and Gosse, 2009; Moreiras and Sepúlveda, 2015), reinforcing the hypothesis of shallow crustal earthquakes as the most likely source of large rockslides in the region, which is consistent with our results.

6.1. Limitations of the model

Uncertainty in the original slope geometry and the validity of the adopted 2D profile to represent the 3D behavior of the rock slope can limit the accuracy of the model, due to small changes in the rockslide volume and the failure mechanism.

Weather conditions in the Andes Cordillera can cause snowing and raining during the winter season. The likely presence of water and high water pressures can aggravate the static and dynamic rock slope stability, modifying the joint resistance and global stress conditions.

The numerical model is unable to capture the failure sequence; however, the simulation outputs show plastic behavior in a significant number of elements near the rock bridge, from the upper surface to the bridge. Considering that some material weakening could occur during small magnitude earthquakes, we hypothesize that the rockslide could have been the sum of a series of events that progressively deteriorated the slope (Eberhardt et al., 2004, 2016). However, we did not perform numerical simulations that considered for this effect.

We did not include the minor sets of discontinuities and rock mass fractures in the numerical model. Although the slope failure was controlled by the modeled sliding planes, these features can aggravate the slope instability due to material deterioration (Stead et al., 2004).

7. Conclusions

Results from the numerical modelling indicate that the rock slope is statically unstable when the joints that form the sliding planes are considered open with the Barton-Bandis constitutive model and the rock mass is modeled with an elasto-plastic constitutive law. We inferred that at least one rock-bridge is required to ensure the slope static stability.

The dynamic response of the rock slope with one rock bridge was tested considering 100 horizontal acceleration records from the Northridge, the Chi Chi, and the Kobe earthquakes as input motions. The numerical model predicts for these inputs a pronounced topographic amplification at the rock slope with respect to a reference point at the base of the slope. The trend indicates that the peak acceleration in the rock slope more than doubles the value calculated at the reference point. In addition, the peak acceleration, the peak velocity, and the Arias Intensity calculated in the center of gravity of the rockslide highly correlate with the rockslide displacement. Other variables such as the significant duration and the peak frequency of the input and recorded acceleration time-histories show poor correlation with the displacement of the rockslide. There is no apparent correlation between the slope vibration modes and the input signals dominant frequencies in the relative displacement. Our analyses identified that a relative displacement along the sliding surface larger than 20 m result in complete rock slope failure. The combined application of horizontal and vertical input motions does not aggravate the displacements along the sliding surfaces provided the horizontal peak accelerations are larger than the vertical ones.

Acknowledgements

This work was funded by a Conicyt Fondecyt Regular Research grant (No. 1140317), and NERC-Newton Fund grant NE/N000315/1. LiDAR data was kindly provided by T. Oppikofer and R.L. Hermanns from the Norwegian Geological Survey. We greatly acknowledge to Professor S. Rebolledo and S. Moya from the Department of Geology at the University of Chile for their collaboration in the field campaigns and analyses.

Appendix A. Supplementary data

Supplementary data to this article can be found online at https://doi.org/10.1016/j.enggeo.2018.02.001.

References

Alameda-Hernández, P., Jiménez-Perálvarez, J., Palenzuela, J.A., El Hamdouni, R., Irigaray, C., Cabrerizo, M.A., Chacón, J., 2014. Improvement of the JRC calculation using different parameters obtained through a new survey method applied to rock discontinuities. Rock Mech. Rock. Eng. 47 (6), 2047–2060.

Alvarado, P., Beck, S., Zandt, G., Araujo, M., Triep, E., 2005. Crustal deformation in the south-central Andes backarc terranes as viewed from regional broad-band seismic waveform modelling. Geophys. J. Int. 163 (2), 580–598.

Alvarado, P., Barrientos, S., Saez, M., Astroza, M., Beck, S., 2009. Source study and tectonic implications of the historic 1958 Las Melosas crustal earthquake, Chile, compared to earthquake damage. Phys. Earth Planet. Inter. 175 (1), 26–36.

Antinao, J.L., Gosse, J., 2009. Large rockslides in the Southern Central Andes of Chile (32–34.5°S): tectonic control and significance for Quaternary landscape evolution. Geomorphology 104 (3–4), 117–133.

Bahaaddini, M., Hagan, P., Mitra, R., Hebblewhite, B., 2014. Scale effect on the shear behaviour of rock joints based on a numerical study. Eng. Geol. 181, 212–223.

Barrientos, S., Vera, E., Alvarado, P., Monfret, T., 2004. Crustal seismicity in central Chile. J. S. Am. Earth Sci. 16 (8), 759–768.

Barton, N., 1982. Modelling Rock Joint Behaviour From In Situ Block Tests: Implications for Nuclear Waste Repository Design: ONWI-308. 96 Office of Nuclear Waste Isolation, Columbus, Ohio.

Bhasin, R., Kaynia, A.M., 2004. Static and dynamic simulation of a 700-m high rock slope in western Norway. Eng. Geol. 71 (3), 213–226.

Charrier, R., Baeza, O., Elgueta, S., Flynn, J., Gans, P., Kay, S., Muñoz, N., Wyss, A., Zurita, E., 2002. Evidence for Cenozoic extensional basin development and tectonic inversion south of the flat-slab segment, southern Central Andes, Chile (33–36 SL). J. S. Am. Earth Sci. 15 (1), 117–139.

Chen, S., Zhao, J., 1998. A study of UDEC modelling for blast wave propagation in jointed rock masses. Int. J. Rock Mech. Min. Sci. 35 (1), 93–99.

Choi, S.O., Chung, S.-K., 2004. Stability analysis of jointed rock slopes with the Barton-Bandis constitutive model in UDEC. Int. J. Rock Mech. Min. Sci. 41, 581–586.

Chuhan, Z., Pekau, O., Feng, J., Guanglun, W., 1997. Application of distinct element method in dynamic analysis of high rock slopes and blocky structures. Soil Dyn. Earthq. Eng. 16 (6), 385–394.

Contreras, V., Boroschek, R., 2012. Strong ground motion attenuation relations for Chilean subduction zone interface earthquakes. In: Proceedings of 15 World Conference on Earthquake Engineering.

Eberhardt, E., Stead, D., Coggan, J., 2004. Numerical analysis of initiation and progressive failure in natural rock slopes—the 1991 Randa rockslide. Int. J. Rock Mech. Min. Sci. 41 (1), 69–87.

Eberhardt, E., Preisig, G., Gischig, V., 2016. Progressive failure in deep-seated rockslides due to seasonal fluctuations in pore pressures and rock mass fatigue. In: Stefano Aversa, L.C., Picarelli, Luciano, Scavia, Claudio (Eds.), Landslides and Engineered Slopes. Experience, Theory and Practice. Proceedings of the 12th International Symposium on Landslides (Napoli, Italy, 12–19 June 2016). CRC Press, pp. 121–136.

Farías, M., Comte, D., Charrier, R., Martinod, J., David, C., Tassara, A., Tapia, F., Fock, A., 2010. Crustal-scale structural architecture in central Chile based on seismicity and surface geology: implications for Andean mountain building. Tectonics 29 (3).

Flores, R., Arias, S., Jenshke, V., Rosemberg, L.A., 1960. Engineering aspect of the earthquakes in the Maipo Valley, Chile, in 1958. In: Proceedings of Proceedings of 2nd World Conference in Earthquake Engineering. vol. 1. pp. 409–431.

Fock, A., 2005. Cronologıa y tectónica de la exhumación en el Neógeno de los Andes de Chile Central entre los 33° y los 34°S. Tesis para optar al grado de magister en ciencias, mención geología. Universidad de Chile, Santiago, Chile.

Gischig, V.S., Eberhardt, E., Moore, J.R., Hungr, O., 2015. On the seismic response of deep-seated rock slope instabilities — insights from numerical modeling. Eng. Geol. 193, 1–18.

Gischig, V., Preisig, G., Eberhardt, E., 2016. Numerical investigation of seismically induced rock mass fatigue as a mechanism contributing to the progressive failure of deep-seated landslides. Rock Mech. Rock. Eng. 49 (6), 2457–2478.

Gonzalez, P., 2010. Geología y geomorfología del complejo de remociones en masa La Engorda. Memoria para optar al título de geologo. Universidad de Chile, Santiago, Chile.

Hencher, S., Richards, L., 2015. Assessing the shear strength of rock discontinuities at laboratory and field scales. Rock Mech. Rock. Eng. 48 (3), 883–905.

Idini, B., Rojas, F., Ruiz, S., Pasten, C., 2017. Ground motion prediction equations for the Chilean subduction zone. Bull. Earthq. Eng. 15 (5), 1853–1880.

Itasca, 2016. UDEC - Universal Distinct Element Code, Version 6.0 User's Manua. Itasca Consulting Group, Inc., Minneapolis.

Klohn, C., 2015. Geología de la Cordillera de los Andes de Chile Central, Provincias de Santiago, O'Higgins, Colchagua y Curicó. Instituto de Investigaciones Geológicas,

Santiago.
Kveldsvik, V., Kaynia, A.M., Nadim, F., Bhasin, R., Nilsen, B., Einstein, H.H., 2009. Dynamic distinct-element analysis of the 800 m high Åknes rock slope. Int. J. Rock Mech. Min. Sci. 46 (4), 686–698.
Lenti, L., Martino, S., 2012. The interaction of seismic waves with step-like slopes and its influence on landslide movements. Eng. Geol. 126, 19–36.
Leyton, F., Ruiz, S., Sepúlveda, S.A., 2010. Reevaluación del peligro sísmico probabilístico en Chile central. Andean Geol. 37 (2), 455–472.
Lin, Y., Zhu, D., Deng, Q., He, Q., 2012. Collapse analysis of jointed rock slope based on UDEC software and practical seismic load. Proc. Eng. 31, 441–446.
Liu, Y., Li, H., Xiao, K., Li, J., Xia, X., Liu, B., 2014. Seismic stability analysis of a layered rock slope. Comput. Geotech. 55, 474–481.
Lomnitz, C., 1970. Major earthquakes and tsunamis in Chile during the period 1535 to 1955. Geol. Rundsch. 59 (3), 938–960.
Luo, G., Hu, X., Gu, C., Wang, Y., 2012. Numerical simulations of kinetic formation mechanism of Tangjiashan landslide. J. Rock Mech. Geotech. Eng. 4 (2), 149–159.
Mavrouli, O., Corominas, J., Wartman, J., 2009. Methodology to evaluate rock slope stability under seismic conditions at Sola de Santa Coloma, Andorra. Nat. Hazards Earth Syst. Sci. 9 (6), 1763–1773.
Montalva, G.A., Bastías, N., Rodriguez-Marek, A., 2017. Ground-motion prediction equation for the Chilean Subduction Zone. Bull. Seismol. Soc. Am. 107 (2), 901–911.
Moreiras, S.M., Sepúlveda, S.A., 2015. Megalandslides in the Andes of central Chile and Argentina (32°–34°S) and potential hazards. Geol. Soc. Lond., Spec. Publ. 399 (1), 329–344.
Moreno, M., Melnick, D., Rosenau, M., Baez, J., Klotz, J., Oncken, O., Tassara, A., Chen, J., Bataille, K., Bevis, M., Socquet, A., Bolte, J., Vigny, C., Brooks, B., Ryder, I., Grund, V., Smalley, B., Carrizo, D., Bartsch, M., Hase, H., 2012. Toward understanding tectonic control on the Mw 8.8 2010 Maule Chile earthquake. Earth Planet. Sci. Lett. 321–322, 152–165.
Pardo, M., Comte, D., Monfret, T., 2002. Seismotectonic and stress distribution in the central Chile subduction zone. J. S. Am. Earth Sci. 15 (1), 11–22.
Pérez, A., Ruiz, J., Vargas, G., Rauld, R., Rebolledo, S., Campos, J., 2014. Improving seismotectonics and seismic hazard assessment along the San Ramón Fault at the eastern border of Santiago city, Chile. Nat. Hazards 71 (1), 243–274.
Rossel, P., Oliveros, V., Mescua, J., Tapia, F., Mihai, N.D., Calderón, S., Charrier, R., Hoffman, D., 2014. The Upper Jurassic volcanism of the Río Damas-Tordillo Formation (33°–35.5°S): insights on petrogenesis, chronology, provenance and tectonic implications. Andean Geol. 41 (3), 529–557.
Sadigh, K., Chang, C.-Y., Egan, J., Makdisi, F., Youngs, R., 1997. Attenuation relationships for shallow crustal earthquakes based on California strong motion data. Seismol. Res. Lett. 68 (1), 180–189.
Sepúlveda, S.A., Murphy, W., Jibson, R.W., Petley, D.N., 2005. Seismically induced rock slope failures resulting from topographic amplification of strong ground motions: the case of Pacoima Canyon, California. Eng. Geol. 80 (3), 336–348.
Sepulveda, S.A., Astroza, M., Kausel, E., Campos, J., Casas, E.A., Rebolledo, S., Verdugo, R., 2008. New findings on the 1958 Las Melosas earthquake sequence, Central Chile: implications for seismic hazard related to shallow crustal earthquakes in subduction zones. J. Earthq. Eng. 12 (3), 432–455.
Sepúlveda, S.A., Serey, A., Lara, M., Pavez, A., Rebolledo, S., 2010. Landslides induced by the April 2007 Aysén Fjord earthquake, Chilean Patagonia. Landslides 7 (4), 483–492.
Sepúlveda, S., Fuentes, J., Oppikofer, T., Hermanns, R., Moreiras, S., 2012. Analysis of a large-scale, stepped planar failure in the Central Andes uplands, Chile, using roughness profiles from terrestrial laser scanning. In: Eberhardt (Ed.), Landslides and Engineered Slopes: Protecting Society through Improved Understanding. Taylor & Francis Group, London.
Souley, M., Homand, F., 1996. Stability of jointed rock masses evaluated by UDEC with an extended Saeb-Amadei constitutive law. Int. J. Rock Mech. Min. Sci. Geomech. Abstr. 33, 233–244 Elsevier.
Stead, D., Coggan, J., Eberhardt, E., 2004. Realistic simulation of rock slope failure mechanisms: the need to incorporate principles of fracture mechanics. Int. J. Rock Mech. Min. Sci. 41, 563–568.
Stead, D., Eberhardt, E., Coggan, J., 2006. Developments in the characterization of complex rock slope deformation and failure using numerical modelling techniques. Eng. Geol. 83 (1), 217–235.
Sturzenegger, M., Stead, D., 2012. The Palliser rockslide, Canadian rocky mountains: characterization and modeling of a stepped failure surface. Geomorphology 138 (1), 145–161.
Thiele, R., 1980. Hoja Santiago, Región Metropolitana, Carta Geológica de Chile N° 29. Servicio Nacional de Geología y Minería.
Udias, A., Madariaga, R., Buforn, E., Muñoz, D., Ros, M., 2012. The large Chilean historical earthquakes of 1647, 1657, 1730, and 1751 from contemporary documents. Bull. Seismol. Soc. Am. 102 (4), 1639–1653.
Wang, X., Nie, G., Wang, D., 2010. Relationships between ground motion parameters and landslides induced by Wenchuan earthquake. Earthq. Sci. 23 (3), 233–242.
Welkner, D., Eberhardt, E., Hermanns, R.L., 2010. Hazard investigation of the Portillo Rock Avalanche site, central Andes, Chile, using an integrated field mapping and numerical modelling approach. Eng. Geol. 114 (3–4), 278–297.
Wu, Y.-M., Teng, T.-L., Shin, T.-C., Hsiao, N.-C., 2003. Relationship between peak ground acceleration, peak ground velocity, and intensity in Taiwan. Bull. Seismol. Soc. Am. 93 (1), 386–396.
Zhao, X., Zhao, J., Cai, J., Hefny, A., 2008. UDEC modelling on wave propagation across fractured rock masses. Comput. Geotech. 35 (1), 97–104.